Scavengers-driven restructuring of V_O-ZnO to V_O-ZnO/ZnS S-scheme heterojunction for boosting the photocatalytic hydrogen production

Z. L. Li [a,b], X. R. Zhu [b], W. Yan [a,b], L. C. Zhang [a,b], Y. C. Wei [a,b], Y. P. Chen [a,b], Y. E. Xie [a,b], J. Xu [a,b,*]

[a] *School of Physics and Electronic Engineering, Jiangsu University, Zhenjiang, Jiangsu, 212013, P. R. China*
[b] *Jiangsu Engineering Research Center on Quantum Perception and Intelligent Detection of Agricultural Information, Jiangsu University, Zhenjiang 212013, China*

In this study, Na₂S and Na₂SO₃ were used as hole sacrificial agents to induce the transformation of ZnO into a Vo-ZnO/ZnS composite (ZnO-X-RE) during the photocatalytic hydrogen evolution process, generating oxygen vacancies and forming an S-scheme heterojunction. This configuration enhances light absorption and establishes efficient S-scheme charge transfer pathways, suppressing electron-hole recombination. The hydrogen production capacity of the optimized ZnO-700-RE reaches 12.08 mmol·g⁻¹·h⁻¹, 25-fold higher than pristine ZnO. This work elucidates the dual role of hole scavengers in modulating photocatalyst evolution and proposes a strategic route for designing high-performance S-scheme systems.

1. Introduction

Human society's predatory harvesting of fossil fuels has led to severe environmental degradation and looming energy shortages. [1,2]. In response to these issues, hydrogen energy has emerged as one of the most promising and sustainable alternatives, offering high combustion efficiency and producing only clean byproducts [3]. Among the various methods for hydrogen production, such as petroleum pyrolysis, water electrolysis, and microbial fermentation, photocatalytic water splitting using solar energy has garnered considerable attention [4,5]. This approach presents a highly effective means of hydrogen production, potentially alleviating the global energy shortage while minimizing environmental impact. To date, various semiconductor photocatalysts, including TiO₂ [6,7], CdS [8], g-C₃N₄ [9] and SrTiO₃ [10], have been extensively utilized in hydrogen production. Among the photocatalysts. Zinc oxide (ZnO), a widely used n-type semiconductor, is renowned for its favorable properties, including a suitable bandgap structure, non-toxicity, high stability, low cost, and exceptional photocatalytic activity [11-13]. These properties make ZnO an excellent candidate for a wide range of photocatalytic applications [14,15]. Despite these advantages, the inherent limitations of ZnO, such as its inability to efficiently harness sunlight and its propensity for electron-hole recombination, necessitate further optimization to enhance its

performance for practical applications [16-18]. In addition, in reactions, electrons take part in the reaction at the interface, while holes are suppressed [19]. Thus, hole scavengers are commonly introduced during the reaction to release primary photogenerated electrons by providing electrons to bind to the hole first, thus reducing the possibility of recombination. Although sacrificial agents are required in most photocatalytic experiments, experimenters often do not investigate their effects [20]. Many experiments will state the sacrificial agent used without considering the reasons involved in its choice. The report shows that different sacrificial agents play different roles in the reaction process [21], but related research is still very limited at present.

Photocatalytic reactions are predominantly surface processes, so electrons produced by light excitation must be transferred to the surface where the catalytic reaction occurs before recombination takes place [22,23]. In large-sized, defect-free single crystals, this charge carrier migration can occur within femtoseconds, as the relatively simple diffusion path allows for rapid migration of electrons [24]. However, in nanomaterials or heterostructures, the relaxation time is significantly prolonged, extending to several nanoseconds [25]. This extended relaxation time provides sufficient opportunity for the carriers to transfer to the interface and participate in the reaction, rather than recombining in the bulk [24]. For one thing, oxygen vacancies (Ovs) in a single ZnO nanocrystal can effectively slow down or even prevent this recombination by creating localized energy states that capture the electrons or holes, thereby improving the efficiency of photocatalytic reactions [26,27]. As such, the rational design and introduction of defects into ZnO photocatalysts have become a key strategy to improve electron utilization [28,29]. On the one hand, S-scheme heterojunction photocatalysts offer significant advantages in optimizing charge separation efficiency [30]. It has been demonstrated that S-scheme heterojunction photocatalysts can boost charge separation while enhancing the redox potential of photogenerated carriers simultaneously [31]. However, with rationally modulating the Ovs in S-scheme heterojunction photocatalysts still remains a challenge and the function of Ovs completely at the heterointerface of S-scheme is still not clear.

In this study, we present ZnO containing a small number of oxygen vacancies underwent successive transformations to a ZnO/ZnS S-scheme heterojunction photocatalyst with more abundant oxygen vacancies during photocatalytic H_2 generation using Na_2SO_3 and Na_2S as a classic hole scavenger. The newly formed oxygen vacancy and heterointerface enhanced light absorption and triggered additional charge transport pathways, thereby improving charge separation efficiency. This combination of improved charge carrier dynamics and expanded light absorption led to exceptional photocatalytic hydrogen production performance, as well as enhanced stability over prolonged reaction periods. These findings will facilitate the development of new photocatalysts with even greater efficiency.

2. Experimental section

2.1. Chemical

Ethylenediaminetetraacetic acid ($C_{10}H_{16}N_2O_8$), anhydrous zinc acetate ($Zn(CH_3COO)_2$), thiourea (CH_4N_2S), nine-water sodium thiosulfate ($Na_2S \cdot 9H_2O$), and anhydrous sodium sulfite (Na_2SO_3) were all analytical grade agents without any prior treatment.

2.2. Synthesis of ZnO spherical particle

ZnO spherical particles were prepared by hydrothermal method [32]. The procedure is as follows: deionized water (80 mL) was added to a 100 mL Teflon reactor. Then, a mixture of thiourea, anhydrous zinc acetate, and ethylenediaminetetraacetic acid (EDTA) was added to the reactor, with the molar ratios of the materials being 4:4:1. The reactor was subjected to a high temperature of 160 °C for 8 hours. Wait for the device to cool down, the sediment is collected and alternately washed 4 times with ultra-pure water. The product was dried for 6 hours under vacuum condition of 80 °C. Then the dried sample was put into the Muffle furnace for calcining, and the temperature condition of the Muffle furnace was set to 2.5 °C/min, and keep at set temperature for 2 hours. Different samples were prepared by changing the annealing temperature and named ZnO-temperature form according to the temperature.

2.3. Characterizations

The structural properties of specimens were analyzed using a Bruker Phaser X-ray diffractometer with Cu Kα radiation. Morphological characterization was performed via JSM-7001F field emission scanning electron microscopy. A JEM-2100 transmission electron microscope provided TEM results. The surface chemical state analysis was performed using the thermal science K-Alpha XPS system. UV-visible diffuse reflectance spectroscopy (Shimadzu UV2550) was used to characterize the range of light utilization. Photoluminescence behavior was investigated with a JASCO FP-6500 fluorescence spectrometer. Electrochemical assessments were implemented on a CHI660B workstation using a three-electrode configuration (Pt counter, $Hg/Hg_2Cl_2/Cl^-$ reference) in 0.1 M Na_2SO_4 electrolyte.

2.4. Photocatalytic hydrogen evolution tests

The experimental conditions are as follows. 10 mg of sample was dispersed in 80 mL water (0.35 M Na_2S and 0.25 M Na_2SO_3), and sonicated for ten minutes to ensure a uniform slurry. Then, the reaction vessel was flushed with high-purity argon gas to completely replace the air. Before simulated irradiation, the reactor was sealed and stirred. The gas samples were collected every hour and analyzed by a gas chromatograph (GC9720Plus). The light source used in the lighting experiment was a LED lamp of 365nm-520nm. The apparent quantum yield (AQY) is calculated as follows:

$$AQY = \frac{Amount\ of\ released\ hydrogen\ molecules\ in\ unit\ time \times 2}{Number\ of\ incident\ photons\ in\ unit\ time} \times 100\%$$

3. Results and discussion

Figure 1a is a composite diagram. SEM images (Figure 1b) reveal that the ZnO samples exhibit a porous microsphere morphology, and TEM images (Figure 1c, d) show the same, which is beneficial for photocatalytic reactions by offering a large surface area that enhances charge transfer and reactant interaction. Figure 1e is an HR-TEM image, by measuring the lattice spacing of ZnO at 0.247 nm, it conforms to the (1 0 1) plane of hexagonal phase ZnO. As displayed in Figure 1e, the XRD patterns further reveal that the diffraction peaks of ZnO are relatively sharp and well-defined,

with no noticeable broadening, suggesting that the ZnO crystallites possess high crystallinity. Moreover, there are almost no peaks corresponding to any crystal impurities, confirming the high purity of the synthetic catalyst. This suggests that the synthesized catalyst has good crystallinity and purity [33].
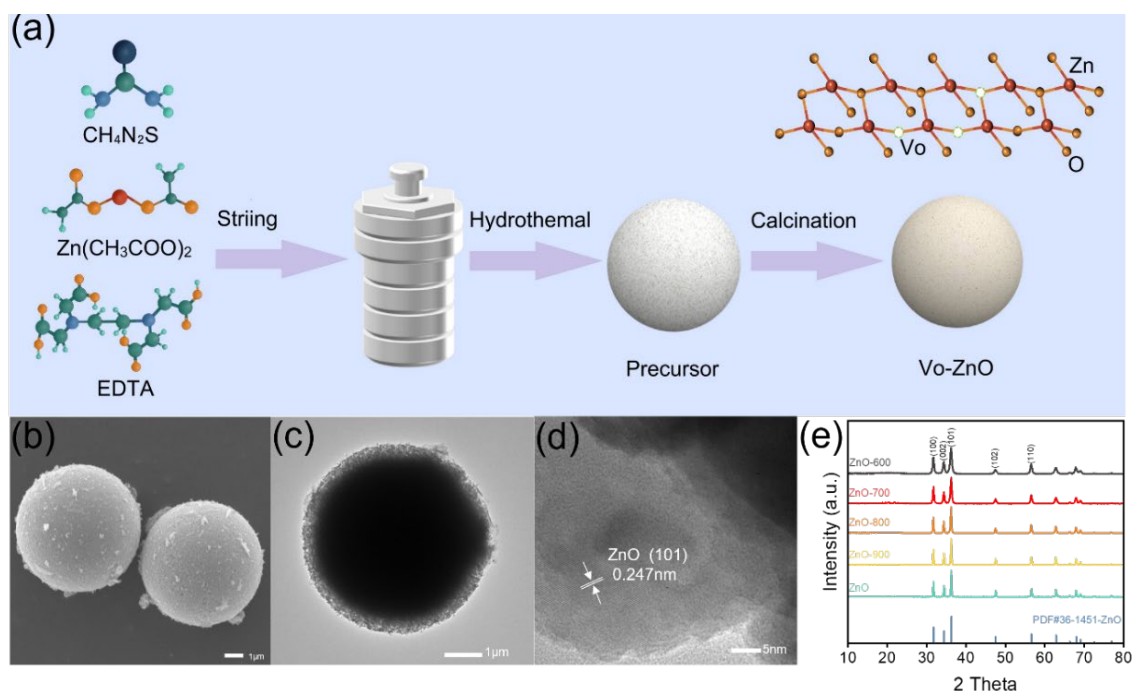

Fig. 1. (a) Experimental preparation diagram of V_O-ZnO. (b) SEM image of V_O-ZnO, (c) TEM image and (d) HR-TEM image of V_O-ZnO. (e) XRD spectrum of synthetic ZnO.

The photocatalytic hydrogen evolution capability of ZnO photocatalysts prepared with Na_2SO_3 and Na_2S as hole scavengers was evaluated. As shown in Figure 2a,b, the hydrogen yield of ZnO is 0.49 mmol·g^{-1}·h^{-1}. In comparison, calcination treatment significantly enhanced the hydrogen production capacity of ZnO, and the precipitation rate of H_2 increases with the increase of calcination temperature. Until the calcination temperature reaches to 700 °C, the H_2 evolution rate reaches to the highest of 12.08 mmol·g^{-1}·h^{-1}, which is approximately 25-fold of pristine ZnO. However, ZnO synthesized at higher calcination temperatures exhibited lower photocatalytic activities, suggesting that a moderate calcination temperature is essential for achieving optimal activity [34]. Due to the high activity of H_2 evolution, ZnO-700 were taken as the photocatalysts afterwards.
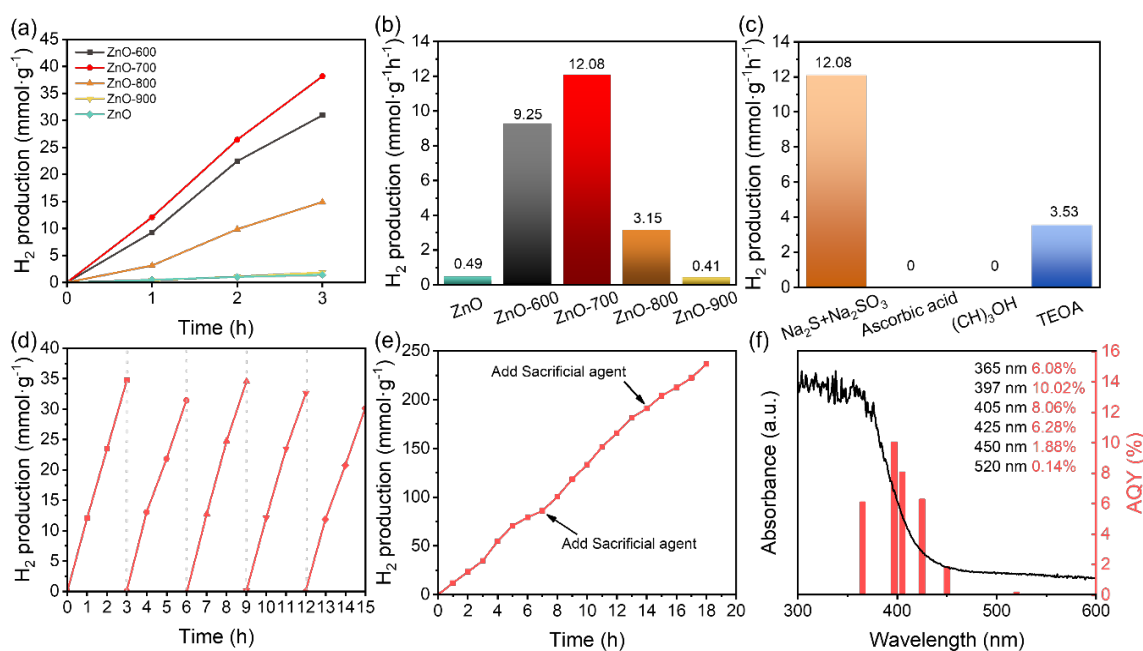
Fig. 2. (a,b) Hydrogen evolution properties of different samples, (c) H₂ production with different sacrificial agents, (d) Cycling stability and (e) Long-term hydrogen production performance of ZnO-700; (f) AQY of ZnO-700 at different wavelengths.

Photocatalysts cyclic stability plays a vital role in their practical application, as it directly influences the long-term performance and reliability of the catalyst under real-world conditions. To assess the cyclic durability of the ZnO-700 catalyst, a series of tests were performed under 397 nm LED light exposure. The same ZnO-700 sample was employed for photocatalytic hydrogen production over five consecutive cycles, with each cycle lasting three hours. The catalyst after each cycle is recovered for the next experiment. Figure 2d shows that hydrogen production capacity remained relatively constant over the five cycles, with no significant decline in performance, indicating the excellent cyclic stability of ZnO-700. Additionally, a long-time experiment was conducted, as illustrated in Figure 2e. The results reveal that the hydrogen production rate increased continuously over an 18-hour period, with a slight decrease observed after approximately 7 hours. The decrease in rate here can be attributed to the loss of sacrificial agents during the reaction. Upon replenishing the sacrificial agents to the initial concentration, the hydrogen production rate returned to its original level, demonstrating that the catalyst maintains its activity over extended periods of operation. These results collectively confirm that the ZnO-700 catalyst exhibits high photochemical stability. The AQY for the photocatalytic H₂ evolution of ZnO-700 was determined under identical conditions. As illustrated in Figure 2f, the trends in AQY variations align well with the DRS spectrum of the ZnO-700 samples. The AQY at 397 nm is calculated to be 10.02%.

To disclose the essentials of sodium sulfide and sodium sulfite, ascorbic acid, methanol and triethanolamine as the hole scavengers were also investigated. As shown in Figure 2c, all three systems have poor hydrogen production capacity. Notably, in all the ascorbic acid, methanol and triethanolamine systems, the catalyst color remained largely unchanged after photocatalystic reaction, whereas, the catalyst color shifted from a light yellow to brown in the sulfide system

(Figure 3a-e). This phenomenon implies that the structure of ZnO is significantly altered during the hydrogen evolution reaction in the presence of Na_2SO_3 and Na_2S. Hydrogen production experiments were further conducted using ZnO-700-RE under the same conditions with different sacrificial agents. As shown in Figure 3f. In the sulfide system, ZnO-700-RE still maintained an excellent hydrogen production capacity of 11.99 $mmol·g^{-1}·h^{-1}$, close to that over ZnO-700. While in triethanolamine and methanol system, ZnO-700-RE exhibited significantly enhanced H_2 evolution rate compared with ZnO-700. Additionally, in the XRD results of ZnO-700-RE (Figure 3g), except for hexagonal ZnO peaks, a new diffraction peak at about 28° can be indexed to the cubic sphalerite phase of zinc sulfide (PDF#05-0566) [35], indicating that ZnS is in situ formed on the ZnO surface during the photocatalytic reaction.
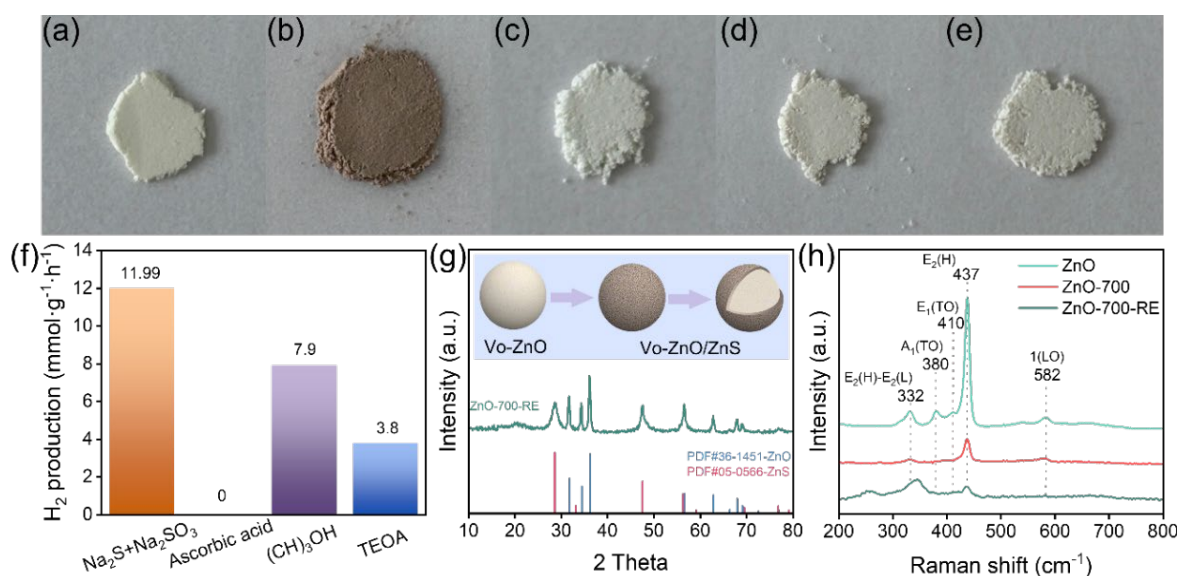

Fig. 3. (a-e) Color changes of ZnO-700 in different sacrificial agent environments (a: ZnO-700, b: Na₂S+Na₂SO₃, c: Ascorbic acid, d: (CH)₃OH, e: TEOA), (f) Hydrogen production rate for ZnO-700-RE with different sacrificial agents, (g) XRD pattern of ZnO-700-RE, (h) Raman spectrum of ZnO-700-RE.

Figure 3h shows the Raman spectrum of the samples obtained using an excitation wavelength of 488 nm, with measurements spanning from 200 to 800 cm^{-1}. The Raman spectrum of ZnO shows the peaks concentrated at 582, 437, 410, 380, and 332 cm^{-1}, which can be identified as 1LO, E_2 (H), E_1 (TO), A_1 (TO), and E_2 (H) - E_2 (L), respectively. The 1LO peak corresponds to the combined A_1 (LO) and E_1 (LO) modes, which are characteristic of ZnO crystals with random orientation [36]. The prominent peak at 437 cm^{-1} is thought to be associated with a high-frequency E_2 mode associated with oxygen atoms, indicating a hexagonal phase of wurtzite [37]. In the Raman spectrum of ZnO-700-RE, additional peaks at 250 cm^{-1}, characteristic of ZnS, are observed in the range of 200 to 350 cm^{-1}, further confirming the presence of ZnS in the samples [38].

In order to have a clearer understanding of the elemental composition of the sample, the electronic chemical states were detected using XPS. The corresponding results are shown in Figure 4. Figure 4d shows the coexist of Zn, O, and S in ZnO-700-RE, while S was not detected in ZnO

and ZnO-700. The appearance of S element in ZnO-700-RE further indicates the occurrence of sulfidation during the reaction process. The high-resolution XPS spectra of the three elements are respectively shown in Figure 4a-c. Figure 4a reveals two peaks at approximately 1145.1 eV and 1022.0 eV, represented by the Zn $2p_{1/2}$ and Zn $2p_{3/2}$, indicating the presence of Zn^{2+} in the catalysts [39]. Figure 4b shows the spectrum of O 1s with two characteristic peaks at 530.3 eV and 531.8 eV, with the former peak representing the lattice oxygen region on the sample surface and the latter corresponding to the defect oxygen region. [40]. The area of the peak at 531.8 eV follows the order ZnO-700-RE > ZnO-700 > ZnO, indicating that the obtained ZnO-700-RE and ZnO-700 possesses more oxygen vacancies than the pristine ZnO. In vacancies-rich ZnO (ZnO-700-RE and ZnO-700), the presence of oxygen vacancy near the Zn site causes the Zn 2p peak to move towards lower binding energy. Meanwhile, no sulfur was detected in ZnO and ZnO-700, and the S 2p peak in ZnO-700-RE was divided into two different peaks at about 162.8 eV and 161.7 eV, which can be considered as S $2p_{1/2}$ and S $2p_{3/2}$ [41]. According to the combined analysis of XRD and XPS data above, ZnO was sulfurized during the reaction process, and in situ generated ZnS.
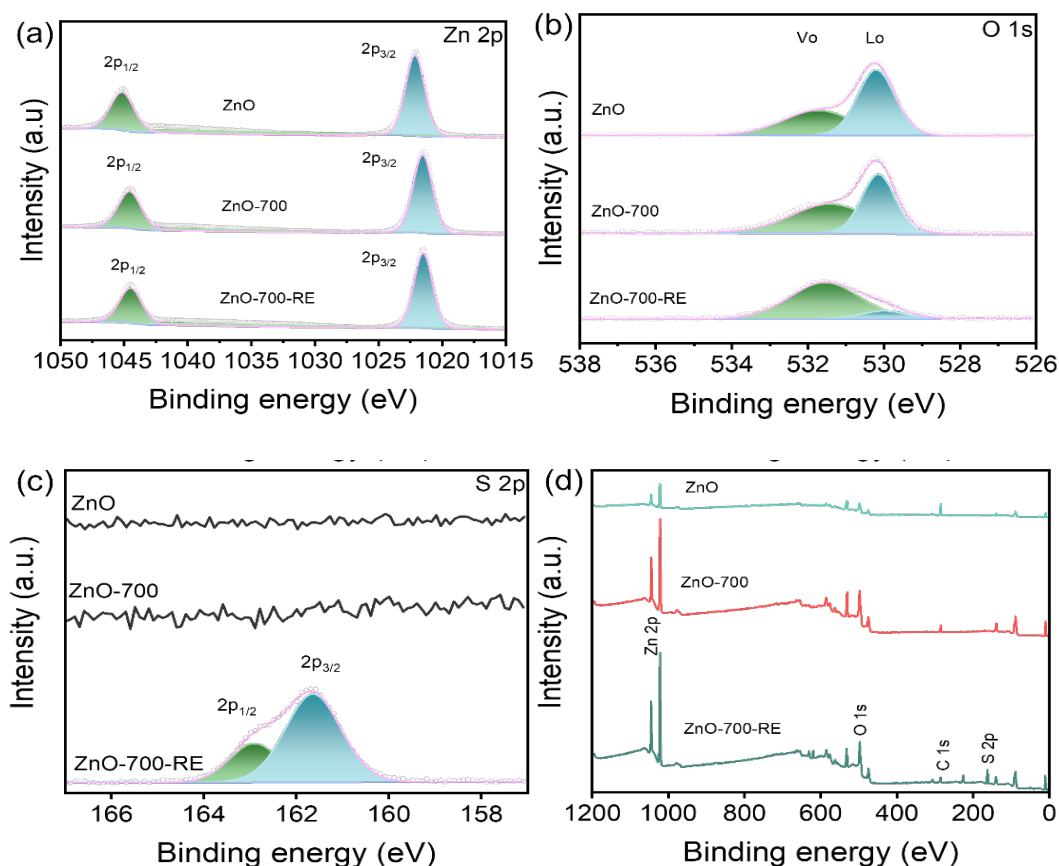

Fig. 4. High-resolution XPS spectra of the three elements (a) Zn 2p, (b) O 1s, and (c) S 2p, (d) XPS survey spectrum of ZnO, ZnO-700, and ZnO-700-RE.

The light absorption capacity of ZnO samples was analyzed by UV-visible DRS. In Figure 5a, all the samples exhibit enhanced light absorption extended absorption edge compared to pure ZnO, which indicates that the utilization rate of light is greatly improved, and the application range of photocatalytic reaction is broadened, especially the utilization of visible light [42,43]. The improvement of light absorption is essential to improve the material's ability to respond to light [44]. Through the correlation formula (Figure 5b), the band gaps of ZnO, ZNO-700 and ZnS were calculated to be 3.19 eV, 3.12 eV and 2.85 eV respectively. [45,46]. The conduction band position of the sample can be measured by the Mot- Schottky method. In the Mott-Schottky plot (Figure 5c), the slopes of ZnO, ZnO-700 and ZnS are all positive, indicating that all the samples belong to n-type semiconductors. The flat band potential of ZnO, ZnO-700 and ZnS are -0.76 V, -0.68 V and -1.35 V (versus NHE) [47]. Generally, the V_{fb} is 0.1 V lower than the CB potential. It can be calculated that the CB potentials of ZnO, ZnO-700 and ZnS are -0.86 V, -0.78 V and -1.45 V, respectively. The valence band positions of ZnO, ZnO-700 and ZnS can be estimated to be 2.33 V, 2.34 V and 1.4 V [48,49], by the formula $E_{VB} = E_{CB} + E_g$. To investigate the electron separation and transfer characteristics, the photoluminescence spectra of pure ZnO, ZnO-700, and ZnO-700-RE were compared at room temperature with laser excitation wavelength of 400 nm. (Figure 5d). The results show that the PL signal strength of ZnO-700 is weaker than that of ZnO [50]. This quenching phenomenon suggests that oxygen vacancies can prevent electrons from recombining with holes, allowing more electrons to participate in the reaction, which is beneficial for photocatalysis [51]. It is also found that the PL strength of ZnO-700-RE is the weakest, which may lead to a reduced probability of electron and hole recombination after vulcanization.
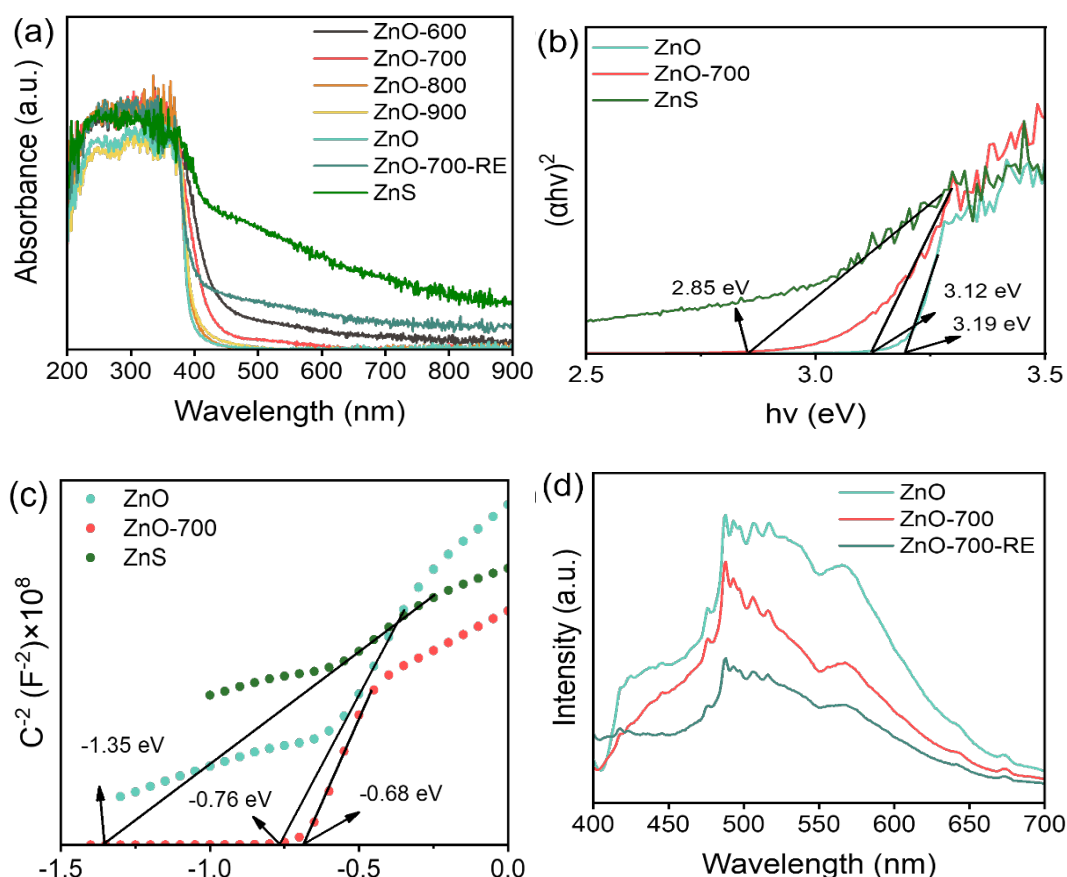
Fig. 5. (a) UV–vis diffuse reflection spectrogram, (b) Kubelka-Munk function vs. the energy of incident light plot, (c) Mott-Schottky plots, (d) PL of catalysts.

According to literature reports, the calculated Fermi level of ZnS is higher than that of ZnO [52]. Due to the height difference between the two Fermi levels, electrons are transferred from ZnS to ZnO through the contact surface between the two until the Fermi level reaches equilibrium, which causes the energy bands of ZnO and ZnS to bend downward and upward, respectively [53,54]. This causes the generation of the internal electric field (IEF), which is directed from ZnS to ZnO. In ZnO, band bending causes electrons to accumulate in the CB at the interface [55,56]. In contrast, in ZnS, the holes in VB cluster at the interface. This results in a strong coulomb attraction between electrons and holes in close positions in ZnO and ZnS. [3]. Furthermore, the presence of IEF will cause the electrons in ZnO to combine with the holes in ZnS [57].
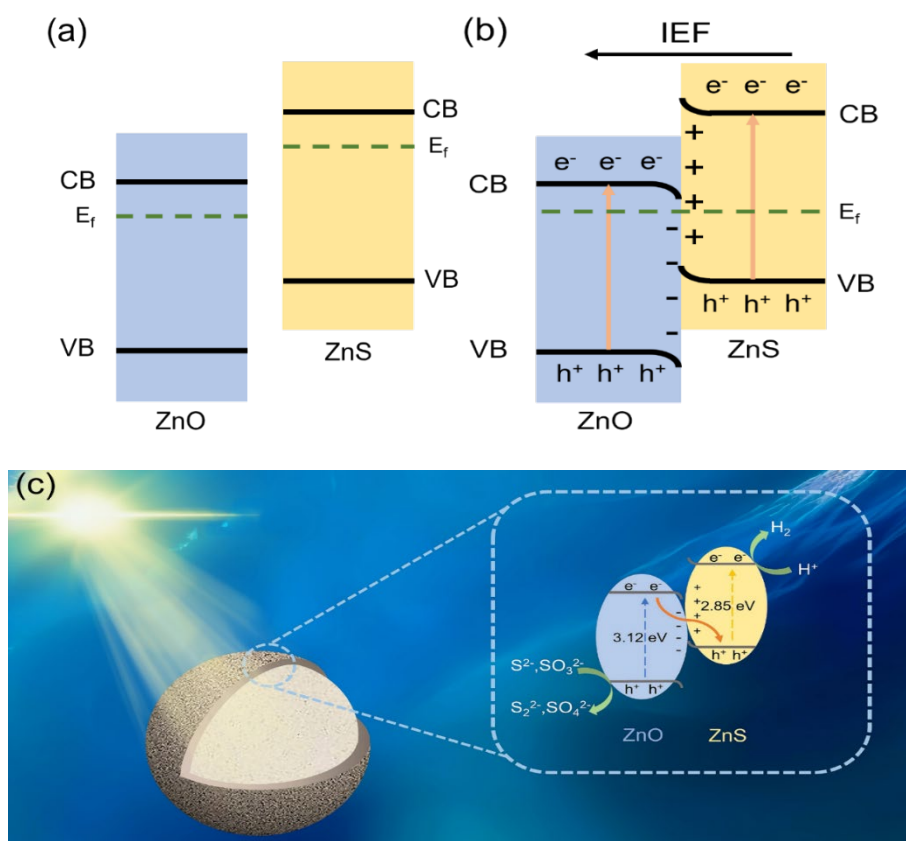
Fig. 6. Schematic of charge transfer mechanism: (a) uncontacted state, (b) binding state, and (c) schematic diagram of photocatalytic mechanism.

Through the analysis and summary of all the test results, we propose a possible way of photocatalytic hydrogen production under the condition of simulated sunlight irradiation. When photoexcitation occurs, ZnO and ZnS simultaneously produce photoexcited electrons and holes. And then under the influence of IEF, the holes in ZnS recombine with electrons in ZnO, resulting in an increase of oxidizing holes in ZnO VB, and an increase of reducing electrons in ZnS CB. Photogenerated electrons in ZnS react with H_2O to produce H_2. At the same time, the sacrificial agent consumes the holes in the VB of ZnO, thereby preventing charge recombination. Finally, it is concluded that the ZnO with oxygen vacancy and the heterojunction formed after vulcanization in the reaction process can not only enhance the light absorption capacity, induce high carrier separation efficiency, and improve redox capabilities, and improve the redox capacity, thus significantly boosting the photocatalytic hydrogen production capacity.

4. Conclusion

In summary, we successfully induced the transformation of ZnO to ZnO/ZnS composites by combining two sulfur-based hole scavengers, during the photocatalysis process. This structural change not only increases the concentration of oxygen vacancies in ZnO, but also enhances light

absorption and creates an S-type charge transfer pathway, which significantly promotes charge separation. The optimized ZnO-700-RE sample demonstrated an impressive hydrogen production rate of 12.08 mmol·g^{-1}·h^{-1}, demonstrating a substantial improvement compared to pristine ZnO. To investigate the alterations in the properties of the prepared catalysts, we employed various characterization techniques. The optimized composite samples show significant advantages, including widening spectral absorption range and decreasing electron-hole recombination rate. These improvements are crucial for optimizing the photoelectrochemical properties and photocatalytic capabilities of the material. This study not only provides valuable experimental support for the significance of hole scavengers in photocatalytic reactions but also presents a viable strategy for constructing efficient S-scheme photocatalysts.

Acknowledgements

References

[1] D. Bahnemann, Solar Energy 77, 445 (2004); https://doi.org/10.1016/j.solener.2004.03.031

[2] T. Su, X. Zhu, Materials 16, 7197 (2023); https://doi.org/10.3390/ma16227197

[3] F. Liu, B. Sun, Z. Liu, Y. Wei, T. Gao, G. Zhou, Chinese Journal of Catalysis 64, 152 (2024); https://doi.org/10.1016/S1872-2067(24)60099-9

[4] H. Zhang, P. Zhang, M. Qiu, J. Dong, Y. Zhang, X. W. Lou, Advanced Materials 31, (2018); https://doi.org/10.1002/adma.201804883

[5] X. Zheng, Y. Song, Y. Liu, Y. Yang, D. Wu, Y. Yang, X. Tian, Coordination Chemistry Reviews 475, 214898 (2023); https://doi.org/10.1016/j.ccr.2022.214898

[6] G. Jia, Y. Wang, X. Cui, H. Zhang, J. Zhao, L. H. Li, W. Zheng, Matter 5, 206 (2022); https://doi.org/10.1016/j.matt.2021.10.027

[7] Z. Yang, X. Zhai, C. Zhang, J. Shi, X. Huang, Z. Li, J. Xiao, Food Hydrocolloids 123, 107187 (2022); https://doi.org/10.1016/j.foodhyd.2021.107187

[8] J. Xu, X. Zhang, W. Yan, T. Xie, Y. Chen, Y. Wei, Inorganic Chemistry 63, 4279 (2024); https://doi.org/10.1021/acs.inorgchem.3c04408

[9] Q. Hao, S. Hao, X. Niu, X. Li, D. Chen, H. Ding, Chinese Journal of Catalysis 38, 278 (2017); https://doi.org/10.1016/S1872-2067(16)62561-5

[10] Y. Jiang, M. Li, Y. Mi, L. Guo, W. Fang, X. Zeng, Y. Liu, Nano Energy 85, 105949 (2021); https://doi.org/10.1016/j.nanoen.2021.105949

[11] L. Zhang, Y. Hu, X. Wang, A. Zhang, X. Gao, A. E.-G. A. Yagoub, C. Zhou, Foods 11, 1656

460

(2022); https://doi.org/10.3390/foods11111656

[12] A. Zhu, T. Jiao, S. Ali, Y. Xu, Q. Ouyang, Q. Chen, Food Chemistry 391, 133277 (2022); https://doi.org/10.1016/j.foodchem.2022.133277

[13] T. Jiao, M. Mehedi Hassan, J. Zhu, S. Ali, W. Ahmad, J. Wang, H. Li, Food Chemistry 337, 127652 (2021); https://doi.org/10.1016/j.foodchem.2020.127652

[14] D. Wu, M. Zhang, B. Xu, Z. Guo, Lwt 135, 110036 (2021); https://doi.org/10.1016/j.lwt.2020.110036

[15] L. Luo, X. Liu, S. Ma, L. Li, T. You, Food Chemistry 322, 126778 (2020); https://doi.org/10.1016/j.foodchem.2020.126778

[16] L. Zhihua, Z. Xue, H. Xiaowei, Z. Xiaobo, S. Jiyong, X. Yiwei, Z. Xiaodong, Food Chemistry 335, 127646 (2021); https://doi.org/10.1016/j.foodchem.2020.127646

[17] Q. Wang, S. Mei, P. Manivel, H. Ma, X. Chen, Current Research in Food Science 5, 868 (2022); https://doi.org/10.1016/j.crfs.2022.05.002

[18] M. Sobhy, S. S. Ali, M. A. Khalil, X. Chen, H. Cui, L. Lin, S. El-Sapagh, Food Control 156, 110117 (2024); https://doi.org/10.1016/j.foodcont.2023.110117

[19] M. J. Berr, P. Wagner, S. Fischbach, A. Vaneski, J. Schneider, A. S. Susha, J. Feldmann, Applied Physics Letters 100, (2012); https://doi.org/10.1063/1.4723575

[20] D. Guerrero-Araque, P. Acevedo-Peña, D. Ramírez-Ortega, R. Gómez, New J. Chem. 41, 12655 (2017); https://doi.org/10.1039/C7NJ02260C

[21] Y. Xu, W. Shan, X. Liang, X. Gao, W. Li, H. Li, X. Qiu, Industrial & Engineering Chemistry Research 59, 4367 (2020); https://doi.org/10.1021/acs.iecr.9b06604

[22] Q. Guan, W. Ran, D. Zhang, W. Li, N. Li, B. Huang, T. Yan, Advanced Science 11, (2024); https://doi.org/10.1002/advs.202401990

[23] T. Yan, N. Li, L. Wang, W. Ran, P. N. Duchesne, L. Wan, G. A. Ozin, Nature Communications 11, (2020); https://doi.org/10.1038/s41467-020-19997-y

[24] G. L. A.L. Linsebigler, J.T. Yates, Chem. Rev. 95, 735 (1995); https://doi.org/10.1021/cr00035a013

[25] W. Yang, M. Gao, Y. Zhang, Y. Dai, W. Peng, S. Ji, W. Xu, Journal of Food Composition and Analysis 136, 106738 (2024); https://doi.org/10.1016/j.jfca.2024.106738

[26] S. Shouket, S. khurshid, J. Khan, R. Batool, A. Sarwar, T. Aziz, F. Zubair Filimban, Food Research International 169, 112940 (2023); https://doi.org/10.1016/j.foodres.2023.112940

[27] N. Mediouni, C. Guillard, F. Dappozze, L. Khrouz, S. Parola, C. Colbeau-Justin, P. Namour, Journal of Hazardous Materials Advances 6, 100081 (2022); https://doi.org/10.1016/j.hazadv.2022.100081

[28] B. Abebe, H. C. A. Murthy, E. Amare, Environmental Nanotechnology, Monitoring & Management 14, 100336 (2020); https://doi.org/10.1016/j.enmm.2020.100336

[29] M. Costa-Silva, F. P. Araujo, Y. Guerra, B. C. Viana, E. C. Silva-Filho, J. A. Osajima, R. Peña-Garcia, Materials Chemistry and Physics 292, 126814 (2022); https://doi.org/10.1016/j.matchemphys.2022.126814

[30] C. Cheng, B. Zhu, B. Cheng, W. Macyk, L. Wang, J. Yu, ACS Catalysis 13, 459 (2022);

https://doi.org/10.1021/acscatal.2c05001

[31] Q. Xu, L. Zhang, B. Cheng, J. Fan, J. Yu, Chem 6, 1543 (2020);
https://doi.org/10.1016/j.chempr.2020.06.010

[32] T. Liu, J. Qian, C. Wang, Y. Wang, Y. Yang, B. Kong, W. Wu, Inorganic Chemistry Communications 119, 108142 (2020); https://doi.org/10.1016/j.inoche.2020.108142

[33] P. Seleš, D. Vengust, T. Radošević, M. Kocijan, L. Einfalt, M. Kurtjak, M. Podlogar, Ceramics International 50, 26819 (2024); https://doi.org/10.1016/j.ceramint.2024.04.410

[34] N. Sharma, R. Jha, S. Baghel, D. Sharma, Journal of Alloys and Compounds 695, 270 (2017); https://doi.org/10.1016/j.jallcom.2016.10.194

[35] H. Ren, K. Ye, H. Chen, F. Wang, Y. Hu, Q. Shi, M. Chen, Colloids and Surfaces A: Physicochemical and Engineering Aspects 652, 129844 (2022); https://doi.org/10.1016/j.colsurfa.2022.129844

[36] Y. Cheng, Z. Chen, P. Yan, J. Shen, J. Kang, S. Wang, X. Duan, ACS Catalysis 14, 4040 (2024); https://doi.org/10.1021/acscatal.3c05554

[37] J. Wang, Y. Xia, Y. Dong, R. Chen, L. Xiang, S. Komarneni, Applied Catalysis B: Environmental 192, 8 (2016); https://doi.org/10.1016/j.apcatb.2016.03.040

[38] J. Zhou, J. Zhao, R. Liu, Applied Catalysis B: Environmental 278, 119265 (2020); https://doi.org/10.1016/j.apcatb.2020.119265

[39] Y. Shundo, T. Tam Nguyen, S. Akrami, P. Edalati, Y. Itagoe, T. Ishihara, K. Edalati, Journal of Colloid and Interface Science 666, 22 (2024); https://doi.org/10.1016/j.jcis.2024.04.010

[40] S. R. Jadhav, S. V. Mohite, C. Lee, J. Bae, R. S. Pedanekar, Y. Kim, K. Y. Rajpure, Sustainable Materials and Technologies 38, e00731 (2023); https://doi.org/10.1016/j.susmat.2023.e00731

[41] Y. Liu, Q. Zhu, M. Tayyab, L. Zhou, J. Lei, J. Zhang, Solar RRL 5, (2021); https://doi.org/10.1002/solr.202100536

[42] Y. Liu, R. Wang, Z. Yang, H. Du, Y. Jiang, C. Shen, A. Xu, Chinese Journal of Catalysis 36, 2135 (2015); https://doi.org/10.1016/S1872-2067(15)60985-8

[43] X. Zhang, X. Yu, J. Wang, Q. Wang, H. Meng, Z. Wang, Food Analytical Methods 11, 2569 (2018); https://doi.org/10.1007/s12161-018-1198-x

[44] Q. Wang, H. Zhou, J. Qian, B. Xue, H. Du, D. Hao, Q. Li, Journal of Materials Science & Technology 190, 67 (2024); https://doi.org/10.1016/j.jmst.2023.11.045

[45] X. Hao, Y. Wang, J. Zhou, Z. Cui, Y. Wang, Z. Zou, Applied Catalysis B: Environmental 221, 302 (2018); https://doi.org/10.1016/j.apcatb.2017.09.006

[46] Y. Xu, W. Zhang, J. Shi, X. Zou, Z. Li, Y. Zhu, Food Chemistry 201, 190 (2016); https://doi.org/10.1016/j.foodchem.2016.01.078

[47] Z. Li, M. Huang, Y. Li, Z. Ai, K. Zhang, X. Yao, X. Hao, Advanced Materials Interfaces 9, (2022); https://doi.org/10.1002/admi.202200066

[48] L. Song, J. Hu, X. Lu, Z. Lu, J. Xie, A. Hao, Y. Cao, Inorganic Chemistry 61, 8217 (2022); https://doi.org/10.1021/acs.inorgchem.2c00632

[49] C. Zhang, Y. Han, L. Lin, N. Deng, B. Chen, Y. Liu, Journal of Agricultural and Food Chemistry 65, 1290 (2017); https://doi.org/10.1021/acs.jafc.6b05305

[50] X. Bi, L. Li, L. Luo, X. Liu, J. Li, T. You, Food Chemistry 385, 132657 (2022); https://doi.org/10.1016/j.foodchem.2022.132657

[51] S. Le, T. Jiang, Y. Li, Q. Zhao, Y. Li, W. Fang, M. Gong, Applied Catalysis B: Environmental 200, 601 (2017); https://doi.org/10.1016/j.apcatb.2016.07.027

[52] J. Jiang, G. Wang, Y. Shao, J. Wang, S. Zhou, Y. Su, Chinese Journal of Catalysis 43, 329 (2022); https://doi.org/10.1016/S1872-2067(21)63889-5

[53] X. Ma, H. Du, M. Tan, J. Qian, M. Deng, D. Hao, H. Zhu, Separation and Purification Technology 339, 126644 (2024); https://doi.org/10.1016/j.seppur.2024.126644

[54] Z. Yu, C. Guan, X. Yue, Q. Xiang, Chinese Journal of Catalysis 50, 361 (2023); https://doi.org/10.1016/S1872-2067(23)64448-1

[55] N. Liang, X. Hu, W. Li, Y. Wang, Z. Guo, X. Huang, J. Shi, Food Chemistry 378, 132076 (2022); https://doi.org/10.1016/j.foodchem.2022.132076

[56] L. Jiang, W. Wei, S. Liu, S. A. Haruna, M. Zareef, W. Ahmad, Q. Chen, Journal of Food Measurement and Characterization 16, 2890 (2022); https://doi.org/10.1007/s11694-022-01401-6

[57] X. Deng, J. Zhang, K. Qi, G. Liang, F. Xu, J. Yu, Nature Communications 15, (2024); https://doi.org/10.1038/s41467-024-49004-7